Research Article | Vol. 30, No. 8 / 11 Apr 2022 / Optics Express 12630

Optics EXPRESS

Deep ultra-violet plasmonics: exploiting momentum-resolved electron energy loss spectroscopy to probe germanium

ZOHREH POURSOTI,[1,7] WENBO SUN,[2,7] SATHWIK BHARADWAJ,[2,7] MAREK MALAC,[3,4] SURAJ IYER,[2] FARHAD KHOSRAVI,[1] KAI CUI,[3] LIMEI QI,[1] NEDA NAZEMIFARD,[1] RAVICHANDRA JAGANNATH,[5] RAJIB RAHMAN,[6] AND ZUBIN JACOB[2,*]

[1] *Department of Electrical and Computer Engineering, University of Alberta, Edmonton, Alberta T6G 2V4, Canada*
[2] *Birck Nanotechnology Center, Elmore Family School of Electrical and Computer Engineering, Purdue University, West Lafayette, Indiana 47907, USA*
[3] *Nanotechnology Research Centre, National Research Council of Canada, Edmonton, Alberta T6G 2M9, Canada*
[4] *Department of Physics, University of Alberta, Edmonton, Alberta T6G 2E1, Canada*
[5] *KLA Corporation, 5 Technology Dr, Milpitas, California 95035, USA*
[6] *School of Physics, University of New South Wales, New South Wales, Sydney 2052, Australia*
[7] *Equal contribution*
[*] *zjacob@purdue.edu*

Abstract: Germanium is typically used for solid-state electronics, fiber-optics, and infrared applications, due to its semiconducting behavior at optical and infrared wavelengths. In contrast, here we show that the germanium displays metallic nature and supports propagating surface plasmons in the deep ultraviolet (DUV) wavelengths, that is typically not possible to achieve with conventional plasmonic metals such as gold, silver, and aluminum. We measure the photonic band spectrum and distinguish the plasmonic excitation modes: bulk plasmons, surface plasmons, and Cherenkov radiation using a momentum-resolved electron energy loss spectroscopy. The observed spectrum is validated through the macroscopic electrodynamic electron energy loss theory and first-principles density functional theory calculations. In the DUV regime, intraband transitions of valence electrons dominate over the interband transitions, resulting in the observed highly dispersive surface plasmons. We further employ these surface plasmons in germanium to design a DUV radiation source based on the Smith-Purcell effect. Our work opens a new frontier of DUV plasmonics to enable the development of DUV devices such as metasurfaces, detectors, and light sources based on plasmonic germanium thin films.

1. Introduction

The plasmonic properties of materials have found a number of applications in the development of photovoltaic devices [1,2], medical sensors [3], perfect absorbers [4,5], lithographic techniques [6], surface enhanced spectroscopy and sensing [7–9]. Obtaining the plasmonic properties of different materials across the electromagnetic (EM) spectrum is of great interest for all such nanophotonic applications [10] (see Fig. 1(a)). Surface plasmons can be observed in graphene in the terahertz regime [11], highly doped III-V semiconductors in the infrared range [12], metallic systems such as copper (Cu) in the visible [13], and heavy metals such as magnesium (Mg) and gallium (Ga) in the ultraviolet region [14]. Observing surface plasmons at much higher energies is a new frontier to design devices in the deep ultraviolet (DUV) regime.

#447017 https://doi.org/10.1364/OE.447017
Journal © 2022 Received 28 Oct 2021; revised 27 Jan 2022; accepted 15 Mar 2022; published 31 Mar 2022

Optics EXPRESS

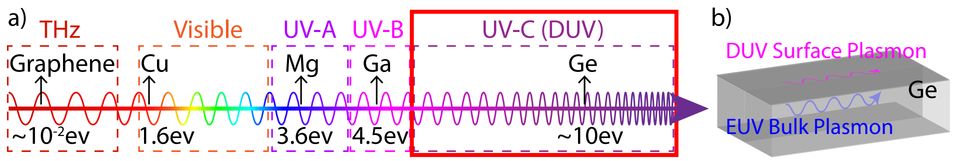

Fig. 1. a) Comparison of surface plasmon frequency in different material systems across the electromagnetic spectrum. b) Schematic display of bulk and surface plasmons in Germanium.

New light sources operating in the extreme ultraviolet (EUV) and deep ultraviolet regions have several potential scientific and industrial applications. DUV and EUV sources are extremely important in semiconductor photolithography techniques. The most popular technique is the immersion lithography [15] which employs excimer laser sources of wavelength 193 nm. Currently, the immersion lithography has been succeeded by EUV lithography through laser-produced plasmon sources [16]. The state of art for lithography is at 13.5 nm, however currently a major interest exists in the development of DUV sources for next generation longer wavelength reticles and wafers [17]. DUV sources also have huge relevance in designing helical drilling systems [18], protein structural analysis [19], and angle-resolved photoemission spectroscopy [20].

In this paper, we explore the plasmonic properties of germanium (Ge) in the DUV regime. We show that Ge supports surface plasmon polaritons (SPP) in the DUV region with its surface plasmon resonance more than twice that of aluminum, a typical material of choice to construct UV devices [21–23]. One can employ DUV plasmons in Ge to construct DUV waveguides, metamaterials, and other devices that are currently not possible with other conventional plasmonic materials. Germanium is a technologically important material thanks to its semiconducting properties at the infrared wavelengths. Counterintuitively, here we show that Ge acts like a Drude-type metal in the DUV region.

We probe the plasmonic properties of Ge using relativistic electrons through momentum resolved electron energy loss spectroscopy (k-EELS). Unlike the traditional electron energy loss techniques [24], in this work both the energy and momentum dispersion of the plasmons are mapped simultaneously [25,26]. This allows us to obtain the plasmonic behavior and the corresponding photonic band spectrum in thin Ge single crystal slabs even as small as 60 nm. The measured photonic band spectrum shows an excellent agreement with the macroscopic electrodynamic electron energy loss theory. Furthermore, we explain the dielectric behavior of DUV plasmons in Ge through first-principles density functional theory (DFT) calculations. Finally, we numerically simulate a Smith-Purcell radiation source (with a wavelength resonance close to 145 nm) in the DUV regime by employing SPP in Ge.

2. DUV plasmons in germanium measured with k-EELS

The DUV plasmonic properties of germanium are measured with relativistic electrons and k-EELS setup in a transmission electron microscope (TEM). Traditional electron energy loss spectroscopy techniques account only for the amount of energy loss of the electron. In k-EELS, the momentum loss information is also obtained by measuring the scattering angle (θ) of the electron after passing through the sample (see Ref. [25] for details on the k-EELS experimental setup). The amount of energy and momentum carried away by the excitations within the sample directly corresponds to the energy and momentum lost by the incident electron. Thus, using k-EELS one can clearly map the photon/polariton band structure [26] and identify photonic excitations such as Cherenkov radiation (CR), waveguide modes, surface and bulk plasmons (BP).

Optics EXPRESS

The samples were prepared via focused ion beam milling (FIB) and mounted on a TEM grid to create free-standing (10 μm × 5 μm) slabs with thickness 60 nm, 100 nm and 200 nm. The focused ion beam milling is conducted through a 40 keV Ga^+ ion beam in a Hitachi NB5000 dual beam instrument, and polished using a 5 keV Ga^+ ion beam to reduce amorphous layer. This is important as we try to observe SPP, as the surface needs to be free of Ga^+ damage as much as possible.

In Figs. 2(a)–(c), we have shown the photonic band spectrum measured using k-EELS for the free standing Ge samples of thicknesses 60 nm, 100 nm and 200 nm, respectively. A flat-band is observed at 16 eV without any dispersion in all three samples. This flat-band is attributed to the BP excitation of germanium. Bulk plasmons occur when $\varepsilon_{\mathrm{Ge}} \rightarrow 0$, which is well into the EUV regime (See Fig. 1). We note that such longitudinal BP oscillations occur at such high energies even in other materials such as aluminum and silicon [25].

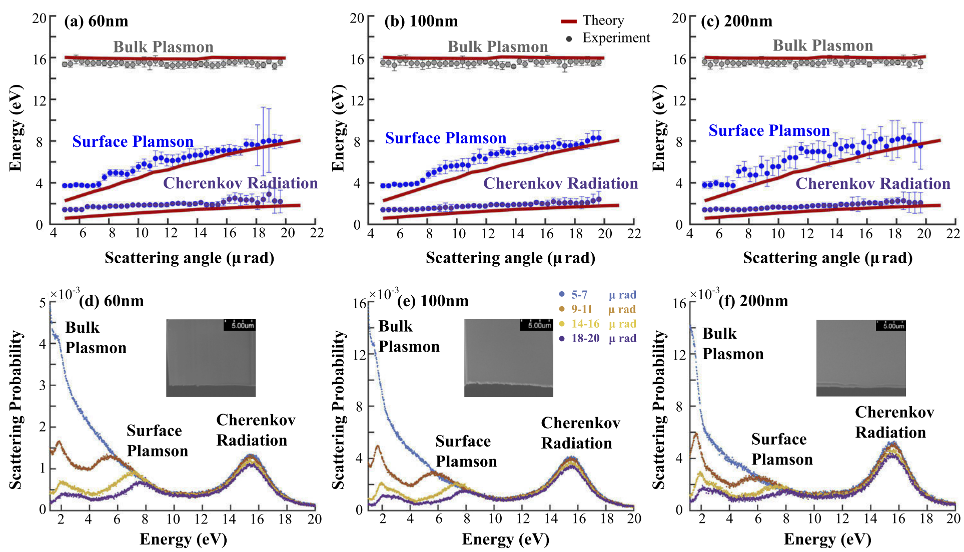

Fig. 2. (a), (b), (c) Photonic band structure of thin germanium samples of thicknesses 60 nm, 100 nm and 200 nm are measured using k-EELS. The dispersionless BP is observed at ∼ 16 eV, the SPP lies at the DUV energy range (4-10 eV) and the CR is observed at 2-4 eV. The solid lines represent the energy-momentum dispersion of the scattered electrons obtained using macroscopic electrodynamic calculations. (d), (e), (f) The electron scattering probability for all three exciations as measured by k-EELS integrated over several scattering angle intervals are plotted as a function of energy for the 60, 100, and 200 nm thin germanium slabs, respectively. A blue-shift is observed for the peak of the surface plasmon with increase in scattering angle for all three samples, whereas no such shift is observed for the bulk plasmon peak. Insets in (d), (e) and (f) display the scanning electron microscope images of the free-standing germanium films prepared via focused ion beam milling (FIB) milling and mounted to the TEM grid.

The highly dispersive bands observed between ≈ 4 − 10 eV in Figs. 2(a)–(c) are the surface plasmon polariton excitations of Ge in the DUV regime. Note that $\omega_{\mathrm{sp}} = \omega_{\mathrm{p}}/\sqrt{2} \approx 11.3$ eV, which indicates that Ge is a Drude-like metal in the DUV. This is in stark contrast with the semiconducting properties of the Ge observed at visible and infrared wavelengths. The highly dispersive nature of SPP bands is further evident in Figs. 2(d)–(f), where we have plotted the scattering probability as a function of energy, obtained within several intervals of scattering angles. We observe a blue-shift in the SPP peak with increase in scattering angle for all three samples, whereas no such shift is observed for the BP peak. In the following, through DFT

Optics EXPRESS

calculations we explain that the metallic nature of Ge in DUV regime is due to the weak interband transitions between valence and conduction bands, which creates unbound valence plasmons that can support SPP excitations.

Bandstructure of Germanium is calculated using HSE06 hybrid functional [28] along *W*-*L*-Γ-*X*-*W* points (see Fig. 3(a)) in the Vienna ab-initio simulation package (VASP) [29]. Hybrid functional approximates the exchange correlation functional by separating electron interaction into long-range and short-range part in the exchange energy. In the DUV region, the interband transition between valence band and conduction band is very weak and the electrons in valence band behave like free electrons which leads to the plasmonic behavior of germanium in the DUV region.

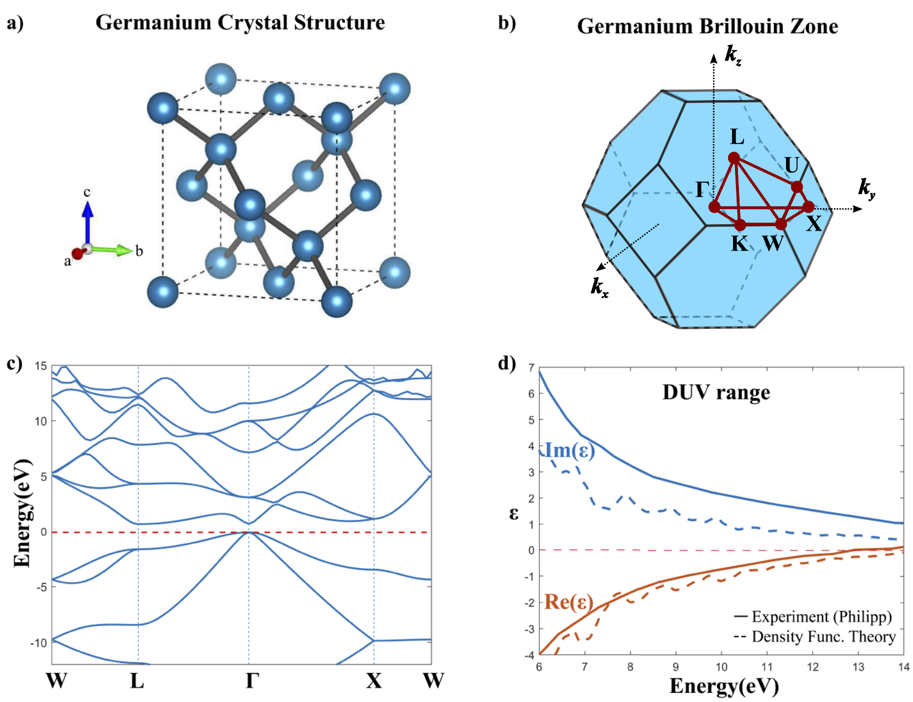

Fig. 3. (a) The face-centered diamond-cubic crystal structure of germanium is shown. (b) The first Brillouin zone and the high symmetry points of the germanium crystal are displayed. (c) Electronic bandstructure of germanium obtained using density functional theory calculations is plotted. (d) Experimental [27] and density functional theory calculation values for the permittivity of germanium are compared. Plot shows the metallic character of germanium in the DUV (ε<0) in the 6–12 eV (103–207 nm) range.

Dielectric function of germanium shown in Fig. 3(d) is calculated using GW_0 & Bethe-Salpeter Equation (BSE) in VASP. GW_0 & BSE takes the excitonic effects into consideration on top of GW_0 results for the electron energy. In the DUV regime, electron-hole pairs are not tightly bound and the dielectric function reduces to a simpler form similar to Drude model with Re(ε)<0. At high frequencies, valence electrons behave as collective oscillations instead of undergoing interband transition. In Ge, due to exhaustion of *f*-sum rule [27] in the DUV region, valance band electrons behave effectively like unbound free electrons and contribute to the observed metallic behavior. For frequencies below the transition frequency between *d*-band and conduction bands, coupling between bounded *d*-band electrons and unbounded valance electrons will not disturb the Drude-like optical response [27].

Further, we compare our experimental data with the simulations of the macroscopic electrodynamic electron energy loss function [30] in Ge for electrons normally incident on the sample. In Fig. 2(a)-(c) we see that the measured data show a strong match with the theoretical calculations (shown in solid lines).

Finally, we observe a low energy branch in the visible range (1.5–2.5 eV) in Fig. 2. Through electron energy loss function theory, we recognize that this low energy branch is the visible CR in germanium. When an electron passes through a medium with a velocity greater than the phase velocity of light in the medium, it generates the CR radiation. Such CR radiation has been observed previously in energy loss experiments [31–33], metamaterials [34,35], and even in two-dimensional materials [36,37]. In dielectrics, CR occurs if the electron velocity is larger than the phase velocity in the medium ($v \geq c/\sqrt{\varepsilon}$). The threshold electron velocity for the relativistic electrons used in our experiment is achieved when $\varepsilon \geq 1.64$. In our k-EELS experiment, the incident electron beam energy is set at 300 keV ($v \approx 0.79c$), which is above the CR radiation threshold.

3. DUV radiation source in germanium

Light-matter interactions mediated through periodic structures have been employed often in stimulating scientific and technological advancements. A worthy objective premised upon the same is to design alternative sources of light. One such phenomenon dependent upon the periodicity of the medium is the Smith-Purcell effect which was first experimentally demonstrated in 1953 [38]. It was observed that the charged particles moving close to a periodic structure at a constant velocity emit electromagnetic waves. In this section, we numerically simulate a DUV radiation source in Ge based on the Smith-Purcell effect.

In a periodic grating structure, non-radiating evanescent surface modes exist near the surface. An electron beam moving above the grating interacts with these evanescent surface modes. As a result, Smith-Purcell radiation is created during this transient process [39]. Smith-Purcell radiation is typically observed in metallic grating structures. For a perfect electric conductor (PEC) grating, the wavelength of the Smith-Purcell radiation is given by [39] $\lambda = (a/g)\,(\cos\theta - 1/\beta)$, where a is the periodicity of the surface and g is the diffraction order (a negative integer), $\beta = v/c$, and θ is the angle of propagation of the emitted electromagnetic wave relative to the initial direction of particle motion.

Smith-Purcell radiation phenomenon can be alternatively understood through the method of image charges. When an electron is moving above a periodic grating structure, the distance between the electron and its image charge has a periodic variation [40]. The resulting oscillating dipole moment created by the electron and its image charge emits the electromagnetic radiation [41]. However, if we pass an electron beam through a hole grating structure (Fig. 4(a)) instead of the electron beam above a periodic grating structure, the number of dipole oscillations is quadrupled, and thereby enhancing the intensity of the radiation in the far-field regime.

We can utilize the metallic behavior of Ge in the DUV region to design Ge based free electron laser source. We propose a hole grating structure made up of Ge as shown in Fig. 4(a). The hole grating structure is constructed to significantly enhance the Smith-Purcell radiation.

To confirm the existence of Smith-Purcell radiation from the Ge based periodic structure, we simulate this laser source by particle-in-cell (PIC) method in CST Studio Suite [42]. In this simulation, a is chosen to be 35 nm with grating hole size 20×20 nm. Electrons pass through the grating structure with a kinetic energy of 20 KeV. Given an electron beam propagating through the grating along the positive x-axis, we analyze the transient and frequency response of the far-field radiation pattern at different observation points. The resulting Smith-Purcell radiation component E_x is plotted as a function of frequency in in Fig. 4(b).

From the spectra of E_x, we find a broad peak with its center close to 8.6 eV (145 nm). Position of this peak matches with the frequency range defined by spectral order $g = -1$ (shown by the

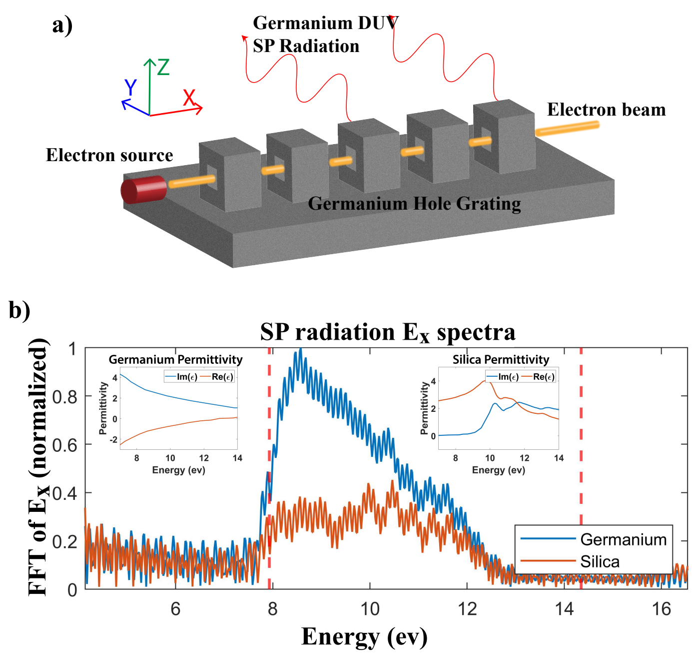

Fig. 4. (a) The schematic diagram depicts the Ge hole grating structure for generating the Smith-Purcell radiation. (b) The fast fourier transform (FFT) of the radiated E_x field component is plotted as a function of frequency for Ge and silica. Smith-Purcell radiation for the hole grating structure is simulated by PIC method in CST [42]. Radiation peak around 8.6 eV (145 nm) is observed in the spectra of E_x for the Ge grating structure. Germanium has a distinctive radiation peak due to its metallic nature in the DUV regime, whereas such a peak is absent in silica. Inset shows the difference in the behavior of dielectric function for both Ge [27] and silica [43] in the DUV regime.

region between two dashed vertical red lines in Fig. 4(b)). Origin of this phenomenon is the metallic behavior of Ge in the DUV region. In order to show the contrast, we also simulated the radiation from the same hole grating structure made with silica. The result is shown by the orange curve Fig. 4(b). We find that the real part of silica's permittivity is positive in this frequency range and as a result, radiation peak in the DUV range is not distinct. Whereas, Ge has negative values of the real part of permittivity in the same range (see inset in Fig. 4(b)), as a result we obtain a radiation peak close to 8.6 eV.

It should be noted that the radiation created by a continuous electron beam is not coherent, and does not have a unique direction. We can easily solve these problems by instead injecting groups of electrons in intervals. The idea is to shape the electrons into groups with a required frequency and pass it through the hole grating structure to create a super-radiant emission [40,44]. With this extension, by using the proposed grating structure made from Ge one can design a coherent unidirectional DUV laser source. This idea will be discussed further in a future publication.

4. Conclusions

We have experimentally demonstrated the existence of DUV surface plasmons in germanium with its resonance energy twice as large as those observed in conventional metals such as aluminum. Through k-EELS technique, we could map the plasmonic excitations in Ge (bulk plasmons, surface plasmonics and Cherenkov radiation) up to a large energy and wavevector values that are not possible through traditional electron energy loss spectroscopy techniques. The measured

Optics EXPRESS

photonic band spectrum has a strong match with the macroscopic electron energy loss theory. We have described the observed metallic behavior of Ge in the DUV region through first-principles density functional theory calculations. Further, we employ the DUV plasmons in Ge to design a DUV radiation source based on the Smith-Purcell radiation phenomena. By passing an electron beam through a Ge hole grating structure, we demonstrated a radiation resonance close to 145 nm. This free electron radiation source has a great potential to be employed in DUV device applications.

5. Methods

k-EELS measurements were performed using a Hitachi HF-3300 TEM/STEM with a cold field emission gun (CFEG), a Gatan Image Filter (GIF) Tridiem^{TM} (model 863) and the MAESTRO central computer control system [45]. An electron beam of energy 300 keV is injected normally onto a thin specimen. EEL spectrometer is used to resolve the electron energy loss over a range of 0-18 eV. The energy-momentum loss of the electrons were mapped to the calibrated CCD to obtain the energy-momentum photonic dispersion in the specified range. Our k-EELS captures the surface plasmon dispersion that are not possible with the earlier EELS techniques. Details of the k-EELS experimental setup and the measurement procedure are described in Ref. [26].

First-principles density functional theory calculations are carried out using Vienna Ab-initio Simulation Package [29]. Germanium bandstructure is calculated through a hybrid functional method with HSE06 functional [46]. To obtain the dielectric function values with a reasonable accuracy, we first perform a single shot GW_0 calculation. A cutoff energy of 180 eV was considered for the expansion of the plane wave basis, and a Γ-shifted $6 \times 6 \times 6$ Monkhorst–Pack [47] grid was used for the sampling of the Brillouin zone with a default Gaussian smearing.

Germanium grating structure as a DUV radiating source is demonstrated based on the simulations using CST Studio by PIC method [42]. Open boundary conditions are applied on all boundaries of the simulation cell. Electron source is placed on one end of the grating structure which generates electrons with a kinetic energy 20 KeV and an effective current 1.6 mA. The x component of the radiated transient electric field (E_x) is analyzed by Fourier transform to obtain the corresponding spectrum. E_x Spectrum is normalized with respect to the peak amplitude at 8.6 eV.

Funding. National Science Foundation (DMR–1654676); Defense Advanced Research Projects Agency (QUEST).

Acknowledgements. MM would like to acknowledge the support from NRC–NANO and University of Alberta. ZP and MM would like to thank Hitachi High-Technologies Canada and Hitachi High-Technologies Japan, in particular Dr. Y. Taniguchi for the excellent support received for a customized Hitachi HF–3300 used in this work.

Disclosures. The authors declare no conflict of interest.

Data availability. Data underlying the results presented in this paper are not publicly available at this time but may be obtained from the authors upon reasonable request.

References

1. H. A. Atwater and A. Polman, "Plasmonics for improved photovoltaic devices," Nat. Mater. **9**(3), 205–213 (2010).
2. S. Pillai and M. Green, "Plasmonics for photovoltaic applications," Solar Energy Materials and Solar Cells **94**(9), 1481–1486 (2010).
3. M. I. Stockman, "Nanoplasmonics: The physics behind the applications," Phys. Today **64**(2), 39–44 (2011).
4. N. Liu, M. Mesch, T. Weiss, M. Hentschel, and H. Giessen, "Infrared perfect absorber and its application as plasmonic sensor," Nano Lett. **10**(7), 2342–2348 (2010).
5. M. Pu, C. Hu, M. Wang, C. Huang, Z. Zhao, C. Wang, Q. Feng, and X. Luo, "Design principles for infrared wide-angle perfect absorber based on plasmonic structure," Opt. Express **19**(18), 17413–17420 (2011).
6. A. Kristensen, J. K. W. Yang, S. I. Bozhevolnyi, S. Link, P. Nordlander, N. J. Halas, and N. A. Mortensen, "Plasmonic colour generation," Nat. Rev. Mater. **2**(1), 16088 (2017).
7. J. P. Camden, J. A. Dieringer, J. Zhao, and R. P. Van Duyne, "Controlled plasmonic nanostructures for surface-enhanced spectroscopy and sensing," Acc. Chem. Res. **41**(12), 1653–1661 (2008).
8. A. J. Haes, C. L. Haynes, A. D. McFarland, G. C. Schatz, R. P. Van Duyne, and S. Zou, "Plasmonic materials for surface-enhanced sensing and spectroscopy," MRS Bull. **30**(5), 368–375 (2005).

Optics EXPRESS

9. R. F. Aroca, "Plasmon enhanced spectroscopy," Phys. Chem. Chem. Phys. **15**(15), 5355–5363 (2013).
10. P. West, S. Ishii, G. Naik, N. Emani, V. Shalaev, and A. Boltasseva, "Searching for better plasmonic materials," Laser & Photonics Reviews **4**(6), 795–808 (2010).
11. L. Ju, B. Geng, J. Horng, C. Girit, M. Martin, Z. Hao, H. A. Bechtel, X. Liang, A. Zettl, Y. R. Shen, and F. Wang, "Graphene plasmonics for tunable terahertz metamaterials," Nat. Nanotechnol. **6**(10), 630–634 (2011).
12. P. Shekhar and Z. Jacob, "Strong coupling in hyperbolic metamaterials," Phys. Rev. B **90**(4), 045313 (2014).
13. D.-D. Wang, C.-W. Ge, G.-A. Wu, Z.-P. Li, J.-Z. Wang, T.-F. Zhang, Y.-Q. Yu, and L.-B. Luo, "A sensitive red light nano-photodetector propelled by plasmonic copper nanoparticles," J. Mater. Chem. C **5**(6), 1328–1335 (2017).
14. J. M. Sanz, D. Ortiz, R. Alcaraz de la Osa, J. M. Saiz, F. González, A. S. Brown, M. Losurdo, H. O. Everitt, and F. Moreno, "Uv plasmonic behavior of various metal nanoparticles in the near- and far-field regimes: Geometry and substrate effects," The Journal of Physical Chemistry C **117**(38), 19606–19615 (2013).
15. D. P. Sanders, "Advances in patterning materials for 193 nm immersion lithography," Chem. Rev. **110**(1), 321–360 (2010).
16. I. Fomenkov, A. Schafgans, and D. Brandt, "Laser-produced plasma sources for high-volume-manufacturing euv lithography," Synchrotron Radiation News **32**(4), 3–8 (2019).
17. A. Cross, K. Sah, V. Anantha, B. Gupta, R. Ynzunza, N. Troy, K. Wu, R. Babulnath, M. Rajendran, D. V. den Heuvel, and P. Leray, "High sensitivity repeater detection with broadband plasma optical wafer inspection for mask defect qualification," in *Extreme Ultraviolet Lithography 2020*, vol. 11517 P. P. Naulleau, P. A. Gargini, T. Itani, and K. G. Ronse, eds., International Society for Optics and Photonics (SPIE, 2020), pp. 53–60.
18. Y. Imamiya, S. Akama, Y. Fujita, and H. Niitani, "Development of microfabrication technology using duv laser," Mitsubishi Heavy Industries Technical Review **53**, 49–54 (2016).
19. Y. Kumamoto, K. Fujita, N. I. Smith, and S. Kawata, "Deep-uv biological imaging by lanthanide ion molecular protection," Biomed. Opt. Express **7**(1), 158 (2016).
20. F.-F. Zhang, F. Yang, S.-J. Zhang, Z. Xu, Z.-M. Wang, F.-L. Xu, Q.-J. Peng, J.-Y. Zhang, X.-Y. Wang, C.-T. Chen, and Z.-Y. Xu, "A picosecond widely tunable deep-ultraviolet laser for angle-resolved photoemission spectroscopy," Chin. Phys. B **22**(6), 064212 (2013).
21. I. Gryczynski, J. Malicka, Z. Gryczynski, K. Nowaczyk, and J. R. Lakowicz, "Ultraviolet surface plasmon-coupled emission using thin aluminum films," Anal. Chem. **76**(14), 4076–4081 (2004).
22. I. Tanabe, Y. Y. Tanaka, K. Watari, T. Hanulia, T. Goto, W. Inami, Y. Kawata, and Y. Ozaki, "Far- and deep-ultraviolet surface plasmon resonance sensors working in aqueous solutions using aluminum thin films," Nature News **7**, 5934 (2017).
23. M. W. Knight, N. S. King, L. Liu, H. O. Everitt, P. Nordlander, and N. J. Halas, "Aluminum for plasmonics," ACS Nano **8**(1), 834–840 (2014).
24. J. A. Scholl, A. L. Koh, and J. A. Dionne, "Quantum plasmon resonances of individual metallic nanoparticles," Nature **483**(7390), 421–427 (2012).
25. P. Shekhar, S. Pendharker, H. Sahasrabudhe, D. Vick, M. Malac, R. Rahman, and Z. Jacob, "Extreme ultraviolet plasmonics and cherenkov radiation in silicon," Optica **5**(12), 1590–1596 (2018).
26. P. Shekhar, M. Malac, V. Gaind, N. Dalili, A. Meldrum, and Z. Jacob, "Momentum-resolved electron energy loss spectroscopy for mapping the photonic density of states," ACS Photonics **4**(4), 1009–1014 (2017).
27. H. R. Philipp and H. Ehrenreich, "Optical properties of semiconductors," Phys. Rev. **129**(4), 1550–1560 (1963).
28. J. Heyd, G. E. Scuseria, and M. Ernzerhof, "Hybrid functionals based on a screened coulomb potential," The Journal of Chemical Physics **118**(18), 8207–8215 (2003).
29. G. Kresse and J. Furthmüller, "Efficient iterative schemes for ab initio total-energy calculations using a plane-wave basis set," Phys. Rev. B **54**(16), 11169–11186 (1996).
30. C. H. Chen and J. Silcox, "Calculations of the electron-energy-loss probability in thin uniaxial crystals at oblique incidence," Phys. Rev. B **20**(9), 3605–3614 (1979).
31. C. H. Chen, J. Silcox, and R. Vincent, "Electron-energy losses in silicon: Bulk and surface plasmons and Čerenkov radiation," Phys. Rev. B **12**(1), 64–71 (1975).
32. R. F. Egerton, *Electron energy-loss spectroscopy in the electron microscope* (Springer, 2011).
33. Q. Meng, L. Wu, H. L. Xin, and Y. Zhu, "Retrieving the energy-loss function from valence electron energy-loss spectrum: Separation of bulk-, surface-losses and cherenkov radiation," Ultramicroscopy **194**, 175–181 (2018).
34. V. Ginis, J. Danckaert, I. Veretennicoff, and P. Tassin, "Controlling cherenkov radiation with transformation-optical metamaterials," Phys. Rev. Lett. **113**(16), 167402 (2014).
35. J.-K. So, J.-H. Won, M. A. Sattorov, S.-H. Bak, K.-H. Jang, G.-S. Park, D. S. Kim, and F. J. Garcia-Vidal, "Cerenkov radiation in metallic metamaterials," Appl. Phys. Lett. **97**(15), 151107 (2010).
36. I. Kaminer, Y. T. Katan, H. Buljan, Y. Shen, O. Ilic, J. J. López, L. J. Wong, J. D. Joannopoulos, and M. Soljacic, "Efficient plasmonic emission by the quantum Cerenkov effect from hot carriers in graphene," Nat. Commun. **7**(1), ncomms11880 (2016).
37. Y. Zhang, C. Hu, B. Lyu, H. Li, Z. Ying, L. Wang, A. Deng, X. Luo, Q. Gao, J. Chen, J. Du, P. Shen, K. Watanabe, T. Taniguchi, J.-H. Kang, F. Wang, Y. Zhang, and Z. Shi, "Tunable Cherenkov Radiation of Phonon Polaritons in Silver Nanowire/Hexagonal Boron Nitride Heterostructures," Nano Lett. **20**(4), 2770–2777 (2020).
38. S. J. Smith and E. M. Purcell, "Visible light from localized surface charges moving across a grating," Phys. Rev. **92**(4), 1069 (1953).

39. P. M. van den Berg, "Smith–purcell radiation from a point charge moving parallel to a reflection grating," J. Opt. Soc. Am. **63**(12), 1588–1597 (1973).
40. P. Zhang, Y. Zhang, and M. Tang, "Enhanced thz smith-purcell radiation based on the grating grooves with holes array," Opt. Express **25**(10), 10901–10910 (2017).
41. A. Gover and Z. Livni, "Operation regimes of cerenkov-smith-purcell free electron lasers and t.w. amplifiers," Opt. Commun. **26**(3), 375–380 (1978).
42. CST Studio Suite, "Cst particle studio," (2010).
43. L. V. R. de Marcos, J. I. Larruquert, J. A. Méndez, and J. A. Aznárez, "Self-consistent optical constants of sio2 and ta2o5 films," Opt. Mater. Express **6**(11), 3622–3637 (2016).
44. H. L. Andrews, C. H. Boulware, C. A. Brau, and J. D. Jarvis, "Superradiant emission of smith-purcell radiation," Phys. Rev. ST Accel. Beams **8**(11), 110702 (2005).
45. M. Bergen, M. Malac, R. McLeod, D. Hoyle, Y. Taniguchi, T. Yaguchi, J. Chen, and T. Yotsuji, "Centralized instrument control for a tem laboratory," Microsc. Microanal. **19**(S2), 1394–1395 (2013).
46. A. V. Krukau, O. A. Vydrov, A. F. Izmaylov, and G. E. Scuseria, "Influence of the exchange screening parameter on the performance of screened hybrid functionals," The Journal of Chemical Physics **125**(22), 224106 (2006).
47. H. J. Monkhorst and J. D. Pack, "Special points for brillouin-zone integrations," Phys. Rev. B **13**(12), 5188–5192 (1976).